Single- and Multi-Beam Drilling of Thin Titanium Foils by Femtosecond Laser Ablation in Liquids

Philipp L. Maack*, Cemal Esen, and Andreas Ostendorf

Applied Laser Technologies, Ruhr University Bochum, Universitätsstraße 150, 44801 Bochum, Germany
**Corresponding author's e-mail: philipp.maack@ruhr-uni-bochum.de*

Ultrashort pulsed laser ablation is an excellent process for high precision micromachining of thin substrates across a broad range of solid materials. As a special application, this method is used in laser drilling to create functional surfaces, e.g. porous materials for filtration or electrodes for electrolysis. This study proposes a different physical alternative to conventional pulsed laser drilling by transitioning the process from a gaseous atmosphere to a denser and thermally more conductive liquid medium. To overcome physical limitations from a low plasma energy threshold and time-related impediments associated with pressure wave and cavitation bubble formation, this study explores different pulse energies at 1032 nm central wavelength with MHz and GHz burst technology and a combined process parallelization through multi-beam generation with a high-power spatial light modulator. Utilizing laser bursts, hole densities of $924 / \mathrm{mm}^2$ with diameters as small as 2 micrometers can be generated over large areas of up to $2500\ \mathrm{mm}^2$. In combination with multi-beam processing, the effective drilling time can be reduced below $5\ \mathrm{ms} / \mathrm{hole}$ for a total of 9 parallel beams. All tests were conducted on 25 micrometer thin foils of titanium grade 1, immersed in flowing deionized water.
DOI: 10.2961/jlmn.2024.03.2004
Keywords: titanium, ultrashort, laser ablation, liquids, drilling, bursts, spatial light modulator

1. Introduction

The process of drilling holes into solid materials by applying force and relative motion through trepanation or rotational movement is considered one of the oldest techniques developed by human mankind, dating back thousands of years. Throughout countless technical advancements in the following centuries, manual drilling of coarse holes has been refined to high technology processes, using different approaches for various applications, materials, and dimensions. While conventional mechanical drilling methods are best suited for high material removal rates and dimensions above a few hundred micrometers, downsized micromachining applications mostly rely on ablation through light-matter interactions and are not restrained by the materials' mechanical properties, such as hardness or ductility. By using femtosecond laser pulses instead of nanosecond pulses or continuous irradiation, energy dissipation into the surrounding material is vastly reduced, which is commonly regarded as cold laser ablation. Although this assumption is applicable for low energy doses from small number of consecutive laser pulses, undesired heat accumulation from a combination of high pulse energies and repetition rates may enlarge the heat affected zone. Consequently, a single compromised microstructure may impede the functionality of the whole machined part. While application dependent parameter optimization and artificial sequencing of machining patterns show great potential in thermal relief through a non-centralized heat input [1], these approaches only tend to counteract the symptoms and not the source of the physical problem. After thermalization, heat conduction into the solid base material is much higher than into the surrounding gaseous medium. Replacing the gaseous medium with a denser and therefore thermally more conductive liquid enables enhanced heat convection and removal of ablated matter, representing a more promising approach on a physical level. This process, commonly known as laser ablation in liquid-phase (LAL), emerged towards the end of the 20th century to generate colloids and nanoparticles from submerged substrates by incubating laser ablated matter within a spatially and temporally confined plasma, characterized by high temperature and pressure [2]. Since the early discovery of its additional potential for quality improvements in micromachining, LAL was adopted for specialized micromachining applications, such as water jet-guided cutting [3]. Compared to conventional laser ablation within a gaseous atmosphere or vacuum, a flowing liquid enhances heat convection and removal of ablated debris. As a result, thermal stresses, and remelting of particles within adjacent regions around the ablation zone are minimized, marking a crucial aspect in precision machining of delicate micro-structures and large area processing, such as functional surfaces or high porosity filters. While significant improvements in terms of surface quality and geometrical tolerances can be achieved with this technique, temporal acceleration of the drilling process is challenging due to its low plasma threshold. A promising approach for process upscaling, commonly used throughout research and industry, is given by using diffractive optical elements (DOE) or spatial light modulators (SLM) to generate multiple beams [4; 5]. The former optical element usually consists of a transparent material with very high damage threshold, ideally suited for applications with pulsed lasers systems. As its main disadvantage however, the DOE is a static optical element whose parameters cannot be changed. As an emerging alternative, technical advancements in the fabrication of high-power SLM provide high damage

thresholds with the substantial advantage of interchangeable and dynamic diffraction patterns. Depending on the requirements, e.g. patterns of multiple parallel beams, each pixel of the SLM´s display can be individually configured to induce a local phase-shift of the incident wavefront. As a result, the sum of all superimposed phase-shifted wavefronts generates the desired intensity distribution within the focal plane. The results presented in this study are transferred to a fully automated process for the generation of so-called porous transport layers (PTL) from thin titanium foils. The primary goal of the superordinate project is to replace existing solutions from sintered particles or fibers with precisely laser drilled foils for an enhanced process efficiency through better electrical conductivity and hydrodynamic flow characteristics. Further information on PTL can be found elsewhere [6].

2. Methods and Materials

In this study different approaches of ultrashort pulsed percussion laser drilling of thin titanium foils immersed in flowing water were investigated. For the general investigations of the ablation characteristics, conventional single-beam ablation was conducted. Results from these preliminary tests were subsequently transferred onto multi-beam ablation, aiming for an overall improvement in processing efficiency by parallelization. Fig. 1 shows a simplified representation of the optical setup and the processing chamber. The laser system used in this study is a Light Conversion Carbide CB3-40W, capable of delivering pico- and femtosecond laser pulses from single-pulse operation up to 2 MHz repetition rate with additional 63 MHz inter- and 2.5 GHz intra-burst pulse trains. The first harmonic, located at a central wavelength of 1032 ± 10 nm, was used in all experiments along with a pulse duration of $t_p = 193$ fs.

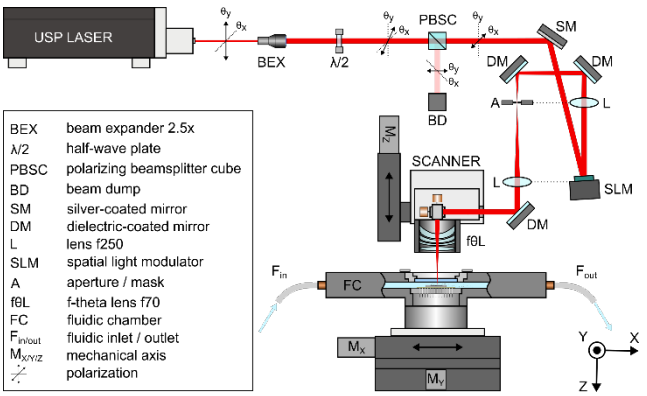

Fig. 1 Simplified schematic of the experimental setup. Laser pulses are emitted by a femtosecond laser system. The initial beam diameter is expanded, and the pulse energy is manually pre-adjusted by a half-wave plate. Depending on the application, controlled phase-shifting of the incident wavefront by a high power spatial light modulator can generate a specific energy distribution of the reflected and superimposed wavefronts within the focal plane. A galvanometer scanner with telecentric f-theta lens focuses the light onto the target surface, which is situated within a fluidic chamber. The optical assembly and fluidic chamber are positioned by high accuracy mechanical axes.

For optimal illumination of the spatial light modulator and reduction of the beam waist within the focal plane, the initial beam diameter was expanded to 10.5 mm by a Sill Optics S6EXP0025-328 beam expander. The maximum pulse energy for laser ablation was manually adjusted by a halfwave plate, deflecting excess radiation by a polarizing beam splitter cube into a beam dump. Within the optical scanner assembly, a folded 4f-setup was used in combination with a water-cooled high-power liquid crystal on silicon spatial light modulator (LCOS SLM) X15223-03BR from Hamamatsu, a Scanlab Excelli Scan 14 galvanometer scanner and a Scanlab 128930 telecentric f-theta objective with a focal length of 70 mm. An aperture mask within the intermediate image plane was used for filtering undesired orders of diffraction during multi-beam processing. Fine positioning of the focal plane was performed by adjusting the optical assembly with a custom motorized mechanical axis. Although the objective´s 26×26 mm^2 typical field-size is sufficient for most experiments, manufacturing of large structures requires precise repositioning of the fluidic chamber. For this purpose, a motorized Linos x.act XY 100 cross slide was used. All mechanical axes are retrofitted with RLS RLC2IC high resolution linear magnetic encoders to guarantee the required positioning accuracy for micromachining.

Fig. 2 shows a sectional view of the processing chamber during an exemplary multi-beam drilling process. For all experiments the same untreated 25 µm thin foil made from grade 1 titanium was used (Ankuro TiGr1 ASTM B265). Prior to laser processing, smaller squares with edge lengths of 55 mm were cut to size and transferred onto a semi-transparent carrier foil with an adhesive top-surface. The foil assembly was then placed onto a flat-machined precision surface within the fluidic chamber. By drawing a vacuum in a subjacent chamber with interconnecting holes, the carrier foil was securely and evenly pressed against the precision surface by the established pressure difference. Additional sealing between vacuum and water was guaranteed by a clamping-ring with integrated labyrinth-seal.

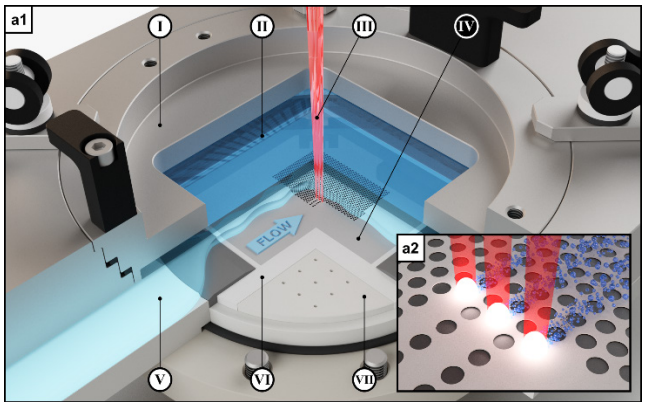

Fig. 2 Sectional view of the processing chamber (a1). The mounting surface is accessible via a sealed lid (I) which holds an integrated anti-reflection coated laser window (II) with a clear aperture of 60×60 mm^2. Single- or multi-beams (III) are used for laser ablation of thin titanium foils (IV) in different experiments. The specimen is immersed in flowing liquid (V) with a constant film thickness and flow velocity within the ablation zone. The specimen is bonded to a carrier foil (VI) which in turn is securely held in place by a vacuum-table (VII). A close-up view (a2) shows an exemplary ablation process by three multi-beams, generated by spatial light modulation.

A water separator within the vacuum assembly compensated for minor water leakages from possible penetration of the carrier foil during laser ablation. After securing the foil assembly, the chamber was closed with a double-sealed lid. During fastening with four knee levers, two opposing mating-surfaces in the lid and chamber functioned as a combined precision stop. This crucial technical measure guaranteed parallelism and the exact same water-film thickness of $t_{H_2O} = 2.50$ mm between the surface of the specified foil and the underside of the laser window that is integrated in the center of the lid. After the chamber was sealed, two pumps in push-pull configuration were slowly displacing all gases with deionized water. After flooding, both pumps were used under full power, delivering a maximum flow rate of $10.5\,\mathrm{l\,min^{-1}}$, corresponding to an average velocity of approximately $760\ \mathrm{mm\,s^{-1}}$ within the laminar flow field. This rate proofed to be sufficient for effective removal of debris and bubbles between two consecutive laser pulses, excluding bursts. In addition to the primary flow cycle, a secondary filtration cycle, consisting of a pressure pump and nanoparticle filters, effectively removed debris, nanoparticles, and colloids from the liquid. A peristaltic pump compressed the residual air in the hermetically sealed fluid reservoir to an absolute pressure of 180 kPa, effectively sealing the system against atmospheric air. Readings from a calibrated pressure sensor are used for a control feedback loop, achieving a relative pressure error of just 2 kPa. Prior to installation, the pressure sensor was calibrated by a certified absolute pressure sensor P502-CI-21KR-AAD-33-V made by Bronkhorst. Pressurizing the system effectively reduced the overall gas contamination by ambient air sucked into the assembly through various small gaps in the fluidic system. Additionally, the amount of persistent gas bubbles from laser processing was reduced through active degassing within the fluid reservoir.

Large area acquisition for determination of hole sizes was done by using a ZEISS Axio Imager A2 which features an automatic image-stitching mode. Comparative measurements for calibration purposes of the former method were done manually by standard confocal light microscopy, using a Nikon ECLIPSE LV100. Scanning electron microscopy (SEM) was conducted with a ZEISS EVO MA 10.

3. Single-beam drilling

Based on a previous study on ultrashort pulsed surface ablation of thin titanium foils immersed in flowing water [7], the fundamental aspects of efficient single-beam percussion drilling in an aqueous environment are presented and discussed in this chapter. In addition, further investigations on optimal burst mode parameters were conducted for additional improvements in ablation efficiency. Subsequently, optimal processing parameters derived from these results were applied to multi-beam processing with up to 9 beams, enabling a manifold enhancement of the process efficiency by parallelization.

The estimated beam-waist diameter d_f for focusing within water can be calculated by adaption of the common equation (1) for focusing within a gaseous environment with Snell's Law of refraction (2).

$$d_f = 2\omega_0 = 4M^2\lambda f \pi^{-1} D^{-1}, \tag{1}$$

$$n_1 \sin\theta_1 = n_2 \sin\theta_2\,, \theta_i = \tan^{-1}(0.5Df^{-1}), \tag{2}$$

$$n_{air} \approx 1, \mathrm{n_{H_2O}} \approx 1.33, M^2 = 1.2, \quad D = 10.8\ \mathrm{mm}, f = 70\ \mathrm{mm}, \lambda_0 = 1030\ \mathrm{nm}. \tag{3}$$

With the given refractive indices n_i, beam propagation ratio M^2, beam diameter D, focal length f, and wavelength λ, the resulting beam diameter was calculated to $d_f \approx 13.88$ µm. A comparative result of $d_f \approx 14.20$ µm was acquired by experimental approximation according to Liu's method [8]. With this technique, the beam waist radius ω_0 can be derived from the spline gradient $\rho \sim {\omega_0}^{-0.5}$ of a logarithmic spline (4) within a semi-log plot of measured radii ${r_0}^2$ as a function of applied energy E_0.

$$r^2 = \rho^2\left(\ln E_0 - \ln E_{r_0}\right). \tag{4}$$

It should be noted that both estimations of the focal point diameter are only valid under ideal conditions without distortion of the wavefront by nonlinear effects. Thus, the latter was conducted only within a range of low pulse energy $E_p = [0\ 0.8]$ µJ. Since the investigated pulse energies in this study expanded beyond these limitations, all following energy-related values in this study are given in pulse energy E_p, instead of the more commonly used units intensity I or fluence Φ, that would need to refer to a specific irradiation area.

3.1 Nonlinear effects

In contrast to conventional laser ablation in gaseous environment and under high vacuum, a combination of different nonlinear effects needed to be considered, that might have substantially impeded the quality and processing time of the ablation process. Most notably, self-focusing, plasma-shielding, and light-scattering on boundary surfaces limited the optimal processing window to low peak pulse energies. Above a critical pulse power, which could be estimated in a range between $P_c = [2.9, 4.3]$ MW for water [9], the optical Kerr effect induced self-focusing. With a given resonator base repetition rate of 2 MHz, equivalent pulse energies ranged between $0.55 - 0.83$ µJ, although these values might vary under the presence of nanoparticles and debris. A more precise estimation of the expected pulse energy threshold can be derived from the depth of self-focusing L_c [10] as the height of the water-film thickness t_{H_2O}.

$$L_c = \frac{0.367\ Z_R}{\sqrt{\left(\sqrt{P_p/P_c} - 0.852\right)^2 - 0.0219}}, \tag{5}$$

$$Z_R = \frac{\pi\, n_{H_2O}\, {\omega_0}^2}{\lambda_0},$$

$$P_p = E_p {t_p}^{-1}.$$

With the given relations for the Rayleigh length Z_R, and average pulse power P_p, equation (5) can be solved for the pulse energy E_p. For the given range of the critical pulse power the calculated pulse energy for an upwards focus-shift due to self-focusing is expected to start within a range

between $0.60 - 0.92$ µJ. This estimation is consistent to the experimentally determined pulse energy threshold for a visible change in ablation efficiency around 0.8 µJ in Fig. 4 and Fig. 5. Fig. 3 illustrates the upward shift of the focal plane into the liquid medium for increasing pulse energies. For low pulse energies (a1) irradiation from the laser was the driving factor in the ablation process, resulting in small hole dimensions with minimal impact on adjacent regions. For increased pulse energies (a2) the upward shift of the focal plane caused a divergent beam propagation below its beam-waist with a significant reduction in the applied fluence onto the target's surface and therefore a considerable decrease in the ablation efficiency. Apart from a drastic distortion of the hole's shape, adjacent surfaces were also impeded by light scattering and plasma. For even higher pulse energies (a3) intense plasma formation within the liquid supposedly lead to a cascade of process impeding phenomena. Diffuse scattering on boundary surfaces of plasma and micro-bubbles, as well as anti-waveguiding of transmitted laser radiation within the plasma was resulting in asymmetrical hole shapes, excessive surface disruption, surface oxidation and an overall poor process stability. To verify the assumption of an energy dependent beam propagation, the focal plane was adjusted depending on the applied pulse energy. Fig. 4 shows the results from an experiment which was set up to determine the optimal focal plane for each pulse energy (a).

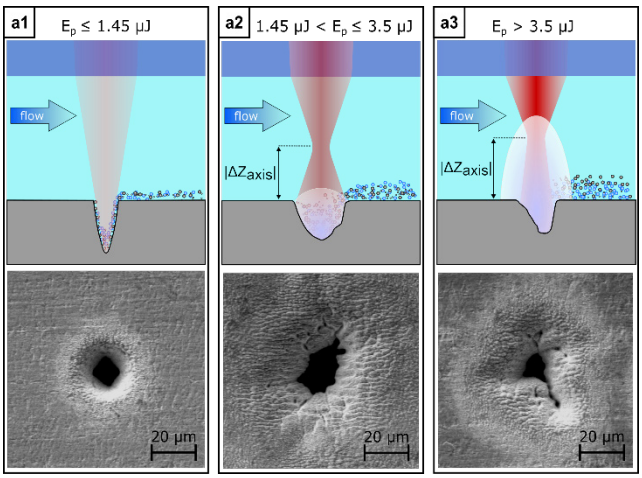

Fig. 3 Upward shift of the focal plane in aqueous environment for increasing pulse energies. Due to the Kerr effect, an upward shift of the focal plane is observed for increasing pulse energies (a1). As a result, a decreased fluence leads to a reduced ablation efficiency and distorted hole shapes (b1, b2). Excessive energy deposition involves plasma-shielding and anti-waveguiding, leading to one-sided bubble ejection and hole deformation (b3). Images from SEM show the impact from different pulse energies on the entrance sides of drilled holes into 25 µm thin titanium foils.

Additionally, a subsequent comparison of a conventional processing strategy with a static position of the optical assembly (b1) and a dynamic adjustment of the focal plane (b2) is shown. Data in Fig. 4 (a) was acquired by drilling identical rows with 40,000 pulses per hole at 500 kHz repetition rate and increasing pulse energy from $0.05 - 5$ µJ. For each pulse energy E_p, a row with 64 holes at different z-axis positions from $+800$ µm to -800 µm relative distance to the estimated focal plane was drilled. For each pulse energy, the black line indicates the best relative axis position, indicating an upward shift of the focal plane for increasing pulse energies. To investigate the different ablation characteristics for a static focal plane and adaptive focusing (b1, b2) each foil was drilled with a total of ten thousand holes in an equilateral 100×100 matrix, where each hole is representing a unique combination of number of pulses and pulse energy. Before evaluation, the foils were cleaned in an ultrasonic bath and rinsed with isopropyl alcohol. After drying and securing between two glass-slides data acquisition was done by high-resolution transmission light microscopy, revealing the shape and area of the exit holes. Since the roundness of a hole is heavily affected by plasma- and bubble formation at higher pulse energies, the more intuitive representation as backside hole diameter would be invalid for higher pulse energies at this stage of the study. The visual representation of the data in Fig. 4 and following experiments gives a great overview of the penetration threshold and hole sizes, as well as the influence on the ablation characteristics from different processing parameters, such as the focal position, repetition rate and burst modes (cf. Fig. 6). Without adaptive focusing, the optimal processing window in (b1) can be estimated around a pulse energy of 0.8 µJ, where the smallest number of pulses is required for a full penetration of the foil's backside (red line).

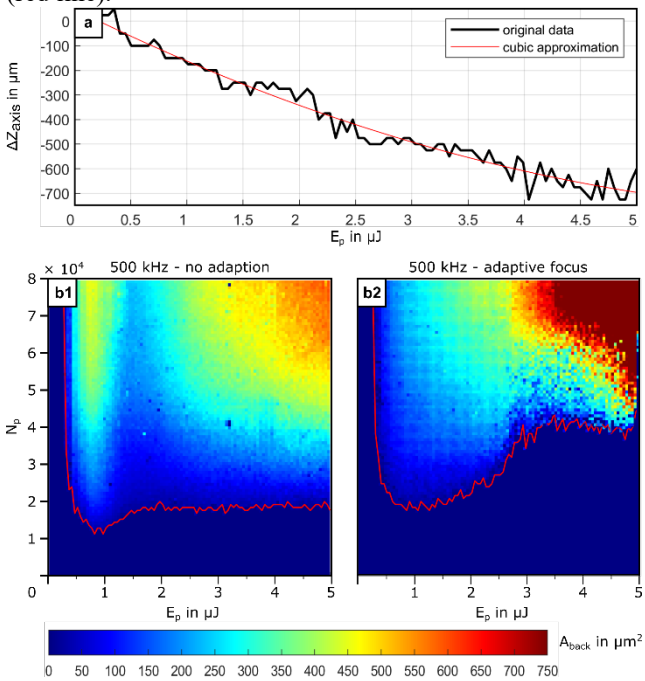

Fig. 4 Influence of energy-dependent automatic focal-plane adaption (a) for the compensation of self-focusing within water (b1, b2). Both images show the drilling process of 100×100 hole arrays with color-represented pierced backside area A_{back}, as a function of different pulse energies E_p and number of subsequent laser pulses N_p. The base frequency of 500 kHz results from a resonator frequency of 2 MHz and a pulse-picking divider of 4. Adaption of the focal plane effectively compensates for an ablation gap situated between 0.8 µJ $- 2.2$ µJ, separating the low-energy region of laser ablation from mostly plasma driven ablation processes.

This value is in accordance with theoretical estimations, calculated by equation (5). The upward shift of the focal plane led to a significant drop in ablation efficiency, dividing

the image into two regions of laser ablation for low pulse energies up to 1.45 µJ and a combination of laser ablation and suspected plasma ablation for higher pulse energies. As shown by the SEM images in Fig. 3 (a2, a3), neither processing time, nor quality improvements can be assigned to the second region. Therefore, operation beyond the optimal pulse energy should be avoided in any case. Using adaptive focusing (b2) closes the gap between the first and second ablation region, verifying the involvement of self-focusing on the ablation characteristics at high pulse energies. The combination of slightly increased optimal pulse energies and higher numbers of pulses resulted in a significant increase in accumulated energy that was required for a full penetration. Thus, it was observed that when using adaptive focusing the overall processing efficiency was decreased both in terms of time and required energy while simultaneously complicating the process from a technical standpoint. Although in this study adaptive focusing was not adopted as a suitable technical measure, it might be necessary for setups with thicker liquid films. In the following experiments, the focal plane was set to the optimal pulse energy of 0.8 µJ.

3.2 Base frequency

Besides the pulse energy and the total number of consecutive pulses, preliminary studies indicated that the pulse frequency have an impact on the ablation rate and hole quality. Fig. 5 shows the influence of different pulse frequencies on the penetration threshold and the size of the pierced backside area, displayed as a color-gradient. The pulse repetition rate was set to the maximum applicable resonator frequency of 2 MHz, termed as 'base frequency' in this study. Lower base frequencies result from setting the internal pulse picker by an integer divider rather than changing the resonator frequency, which guarantees equal pulse parameters. The processed data from different repetition rates shows similar ablation characteristics for different frequencies. Considering the first region, an increasing repetition rate significantly raised the ablation threshold in form of the total number of required pulses to penetrate the backside at a given pulse energy (a1 – a5, $E_p = [0, 1.5\ \mu J]$). Converting the specific pulses for a given repetition rate into time domain (b) reveals almost identical optimal ablation characteristics. Since the accumulated energy is directly proportional to the pulse frequency, it can be concluded that for the nearly identical drilling duration a significant amount of the applied energy is not directly involved in the ablation process when utilizing higher frequencies. This immensely decreasing processing efficiency for increasing repetition rates is typically not observed for laser ablation of metals in gaseous environments. This information is particularly important, since modern femtosecond laser systems often utilize very high repetition rates, which therefore might be used ineffectively without taking appropriate measures for micromachining in liquids. Upon this information, further experiments are targeted specifically in avoiding this negative effect. A possible explanation is given by the generation and lifetime of pressure waves and cavitation bubbles on the nano- to microsecond timescale, that may interfere with subsequent laser pulses applied in short time intervals [11; 12]. A thorough temporal investigation on pressure waves and cavitation bubble dynamics from ultrashort pulse ablation of metal in water can be found elsewhere [13].

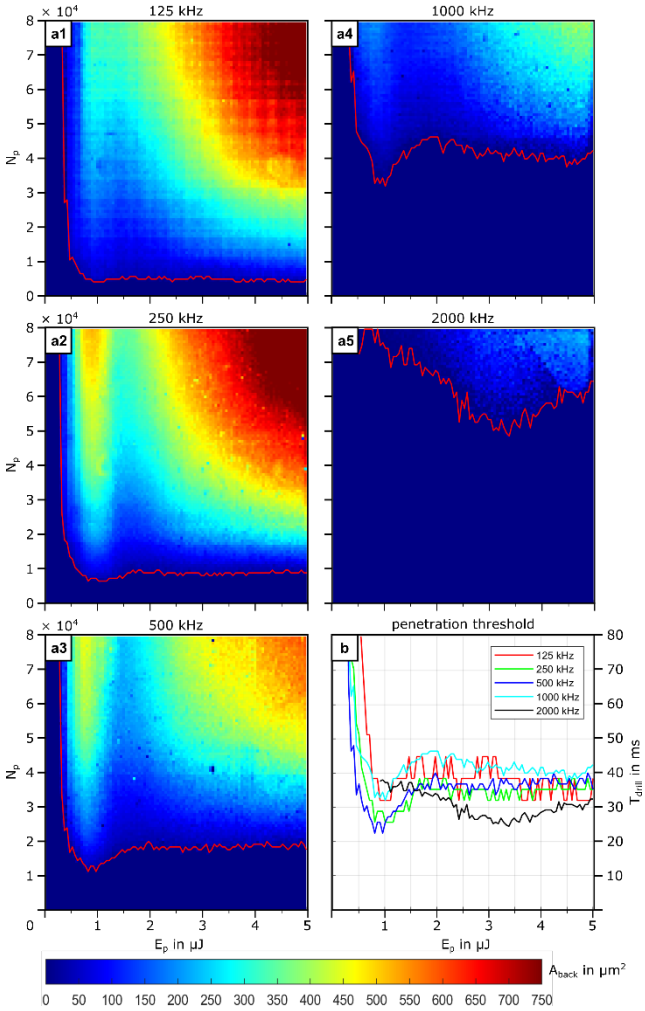

Fig. 5 Influence of different base frequencies f_{base} (a1 – a5) on the drilling process of 100 × 100 hole arrays with color-represented pierced backside area A_{back}, as a function of different pulse energies E_p and number of subsequent laser pulses N_p. To achieve equal pulse shapes for each frequency, all base frequencies are preset by the same resonator frequency of 2 MHz with different pulse picking dividers of 1, 2, 4, 8 and 16.

Contradictory to the results in Fig. 5, much higher frequencies might even improve the process by applying all energy before lattice thermalization and the subsequent formation of pressure waves and cavitation bubbles. Instead of using a different laser system with a much higher resonator frequency, this theory was investigated in the current setup by applying multiple high-frequency bursts trains.

3.3 Burst modes

Utilizing high-frequency bursts for ultrashort pulsed laser ablation in gaseous environment is well-studied and shows great potential for ablation and surface structuring of different materials, like metals [14; 15] and semiconductors [16], resulting in smoother surface texture, deeper ablation cavities and higher ablation rates. Although results from conventional laser ablation in liquids (cf. section 3) revealed

a different ablation characteristic with three separated ablation regions and strong physicochemical interactions, it is suspected that high frequency bursts could be beneficial in applying a high energy dose by multiple pulses, even before the emergence of process impeding pressure waves and cavitation bubbles.

The laser system used in this study can subdivide each pulse into a train of up to ten inter-bursts, which in turn can be further split into ten intra-bursts. An even time distribution of the pulse trains, 16 ns between inter- and 400 ps between intra-bursts, effectively increases the pulse repetition rate in a very short time frame, while the pulse energy is decreased proportionally. Results from the previous tests and preliminary investigations suggested enhanced process efficiencies for smaller base repetition rates. For this reason, the base resonator frequency was altered from 2 MHz to 100 kHz , with two additional frequencies of 50 kHz and 25 kHz by pulse picking. For different numbers of inter- and intra-bursts, the average laser power was adjusted for identical pulse energies, meaning that for an exemplary measurement with the same frequency but subdivision of ten bursts, a tenfold increase in power was required. Similarly, the drill time per hole was adjusted to the total number of pulses, including bursts. Axis labeling for the number of pulses N_p always includes the number of bursts.

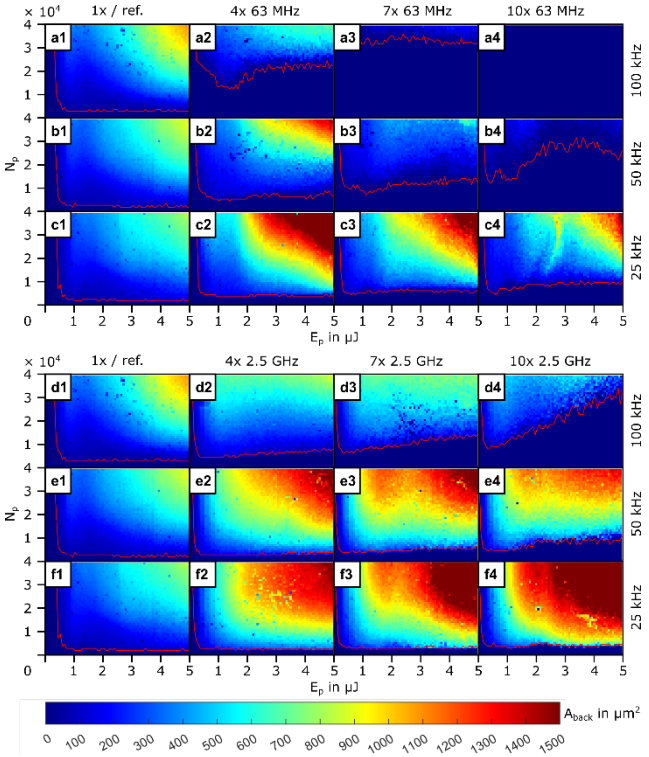

Fig. 6 Influence of different base frequencies f_{base} , burst-frequencies f_{burst} and number of consecutive bursts on the drilling process of 70 × 45 hole arrays with color-represented pierced backside area A_{back}, as a function of different pulse energies E_p and number of subsequent laser pulses N_p. Nanosecond-bursts (a_i, b_i, c_i) show a significant increase in required pulses for a full penetration of a 25 µm thick titanium foil than compared to picosecond-bursts (d_i, e_i, f_i). Additionally, lower base frequencies in combination with higher numbers of bursts show a smaller number of required pulses.

Correspondingly, drilling a hole with a higher base frequency or number of bursts, both decreased the time to reach a desired number of applied pulses. These measures guaranteed an optimal comparability between the acquired datasets from experiments with normal pulse operation to those with inter- and intra-burst modes. The results from the latter are displayed in Fig. 6 as color-represented pierced backside area A_{back}, as a function of different pulse energies E_p and number of subsequent laser pulses N_p. Images $a_1 - f_1$ represent comparative datasets for normal pulse operation without burst-modes. The remaining upper nine images ($a_2 - a_4$, $b_2 - b_4$, $c_2 - c_4$) correspond to inter-bursts with a frequency of approximately 63 MHz while the lower nine remaining images ($d_2 - d_4$, $e_2 - e_4$, $f_2 - f_4$) correspond to high-frequency intra-bursts of about 2.5 GHz. Each of the upper and lower sets is divided into three base frequencies (25 kHz, 50 kHz, 100 kHz) and numbers of subsequent burst pulses (1x, 4x, 7x, 10x). Under normal pulse operation ($a_1 - f_1$), lowering the base frequency did not have a significant impact on the ablation characteristic. When introducing multiple bursts, the ablation characteristics showed a significant change towards lower ablation thresholds and larger sizes of the pierced backside areas. This effect is most noticeable for lower base frequencies (c_i, f_i) and especially for high-frequency intra-bursts (f_2, f_3, f_4). Fig. 7 shows the derived penetration threshold from the same dataset used in Fig. 6, as a function of pulse energy and drilling time for the same base frequencies and numbers of inter- and intra-bursts. Apart from inter-bursts at 100 kHz (a1), all diagrams show a significant reduction in the number of required pulses for a total penetration of the titanium foil at low pulse energies.

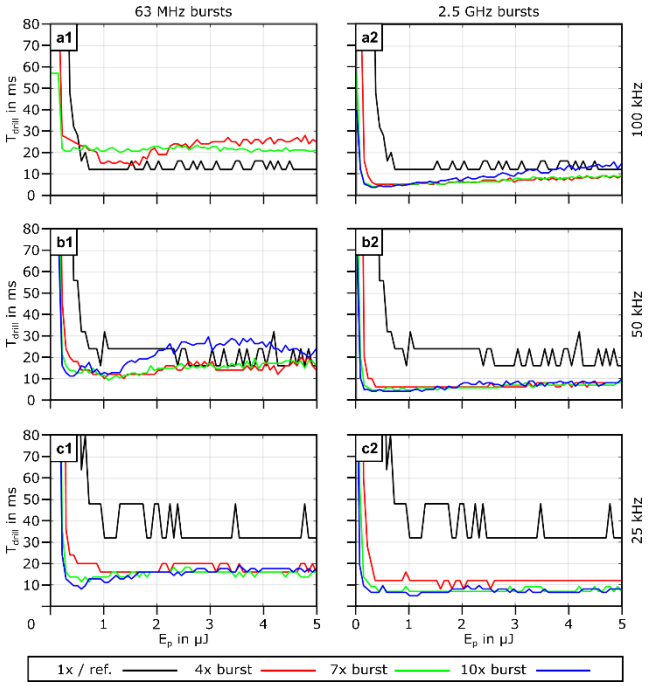

Fig. 7 Influence of different base frequencies f_{base} , burst frequencies f_{burst} and number of consecutive burst pulses N_{burst} on the drilling time T_{drill} for a total penetration of a 25 µm thick titanium foil. Combinations from low base frequencies with high numbers of high-frequency bursts provides best results in terms of energy-usage, energy dependent ablation stability and overall process efficiency (c2 – blue line).

Furthermore, there is a considerable improvement from inter- to the higher frequency intra-bursts. As an example, conventional drilling with a repetition rate of 25 kHz requires a minimum of 32 ms for a total penetration, while a subdivision of each pulse into ten intra-bursts requires merely 4.8 ms. Most notably, changing the time-interval between the pulse trains by choosing a different base frequency only slightly affects the overall time to reach the ablation threshold while simultaneously a much higher energy dose is applied for higher base frequencies and therefore not directly involved in material ablation. Taking a closer look at the time-intervals of different burst frequencies, a pulse train of ten intra-bursts only lasts for about 3.6 ns , while ten inter-bursts stretch over a significantly longer time frame of 144 ns. Within this vastly longer timescale, emergence and lifetime of cavitation bubbles is supposedly located [11], influencing irradiation through diffuse scattering and absorption. This marks a fundamental difference to ablation under gaseous or inert conditions, and therefore posing unique requirements on the precise timing of applied pulses. Using a pulse energy of 0.8 µJ in combination with a low base frequency and the highest available number of ten high-frequency intra-bursts delivered the best results. For these optimal parameters a round hole shape was guaranteed, enabling the replacement of the previously used term of pierced backside area A_{back} by the more intuitive value of pierced backside diameter D_{back}. Fig. 8 shows this value as function of the number of consecutive pulses N_p for all three base frequencies from Fig. 7 (a_2, b_2, c_2 – blue line). Ten identical experiments were conducted for each frequency, displaying each hole diameter within a point cloud with its corresponding arithmetic mean value as a black line. Minimal scattering reveals an excellent process stability with increasing number of pulses.

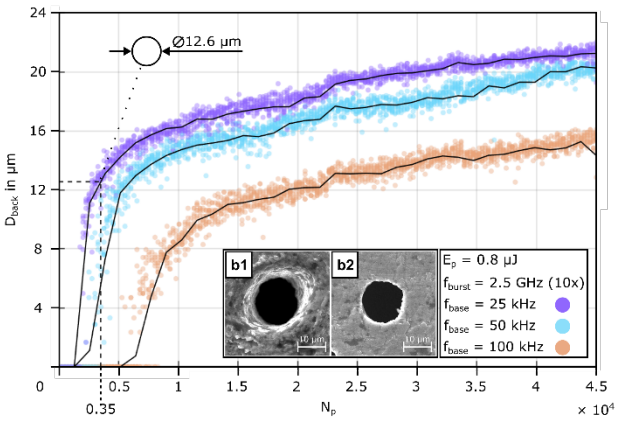

Fig. 8 Influence of the number of consecutive pulses N_p and the base frequency f_{base} on the pierced backside diameter D_{back} for a total penetration of a 25 µm thick titanium foil. Pulse energy E_p, burst frequency f_{burst}, and number of consecutive bursts within a pulse train are constant. For each base frequency the experiment was repeated ten times. Each datapoint is display within a colored point cloud with a black line as arithmetic mean. The diameter and number of pulses have a logarithmic correlation, with slightly larger diameters for lower base frequencies. Low scattering of datapoints indicates a good process stability. Exemplary SEM images of entry (b1) and exit hole (b2) for $N_p = 3500$ reveal excellent roundness, high surface quality and minimal influence on adjacent regions.

As interim conclusion, different recommendations for efficient single-beam percussion drilling of titanium submerged in flowing deionized water can be derived from the results presented in this study. Most importantly, processing within the first ablation region around a narrow pulse energy band centralized at 0.8 uJ is necessary to avoid negative nonlinear effects from self-focusing, plasma-shielding and excessive formation of persistent gas-bubbles. It should be noted that this value might change when using other wavelengths, liquids, and film-thicknesses.

Within Fig. 9 the evaluation of the hole topology reveals significant differences between normal operation and an increasing number of inter- and intra-bursts. The relative ratio between the front and back areas of a pierced hole (purple) shows a slight improvement for high numbers of inter- and a slight degradation for high numbers of intra-bursts, while simultaneously showing a much lower variance for both. For inter-bursts, the ellipticity of the front (green) and back (cyan) is declining, while seven intra-bursts show a slight improvement over normal operation. In all cases, neither a significant improvement, nor decline in ellipticity or aspect ratio could be observed. To optimize the process towards an optimal cylindricity, which is given when all three relative ratios are equal to 1, further improvements on the system must be taken.

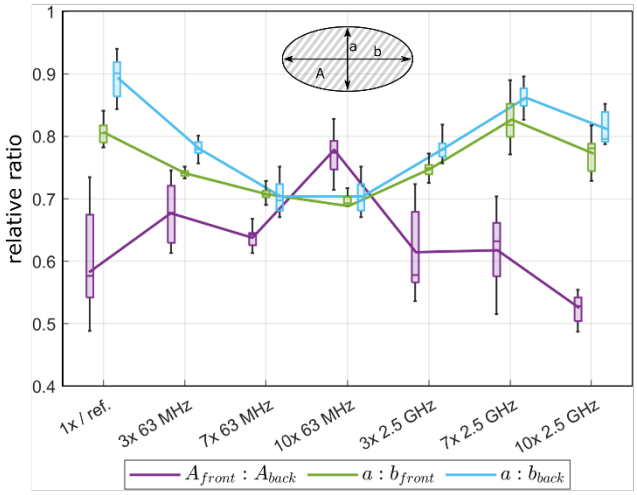

Fig. 9 Influence of different burst modes on the ellipticity of the entry hole $a{:}\,b_{front}$, the exit hole $a{:}\,b_{back}$, and the hole's aspect ratio $A_{front}{:}\,A_{back}$. The base resonator frequency was set to 25 kHz by pulse-picking with a total number of 40.000 pulses per hole. For each datapoint a total of 9 holes were drilled.

Although a definite proof by direct observation is still pending, larger time-intervals between pulse-trains might also reduce the number of large gas bubbles, either through a reduced total energy input per time or fragmentation to less impeding persistent microbubbles. Although directly comparable experiments using high numbers of intra-bursts for ablation within flowing liquids are pending, it can be expected that expanding gases prevent the cavity from filling with liquid during irradiation. Exemplary results from similar studies for drilling within glass under ambient conditions indicate enhanced efficiencies for higher numbers of GHz-bursts [17]. Regarding the technical limitations of the laser system used in this study in terms of maximum number of available bursts pulses, further

improvements at slightly higher numbers of GHz-bursts can be expected, before shielding by cavitation-bubbles may impede the process.

4. Multi-beam drilling

As described in section 3, for efficient single-beam percussion drilling within an aqueous environment many aspects of process impeding phenomena need to be considered. Most importantly, processing around the optimal ablation threshold of 0.8 µJ not only yields the best dimensional quality but also marks the boundary for excessive plasma-formation. Due to this limitation, process enhancements in form of higher ablation rates and overall time-savings cannot be enforced by increasing the pulse energy.

The phase patterns used in this study were calculated by a modified variant of the Gerchberg-Saxton algorithm which is commonly used for iterative phase pattern generation. In contrast to the standard algorithm, an additional suppression of the first order of diffraction was implemented for better intensity homogenization. The flexibility and easy adaptability of these phase patterns gives the SLM a great advantage over the static phase shifting by a DOE.

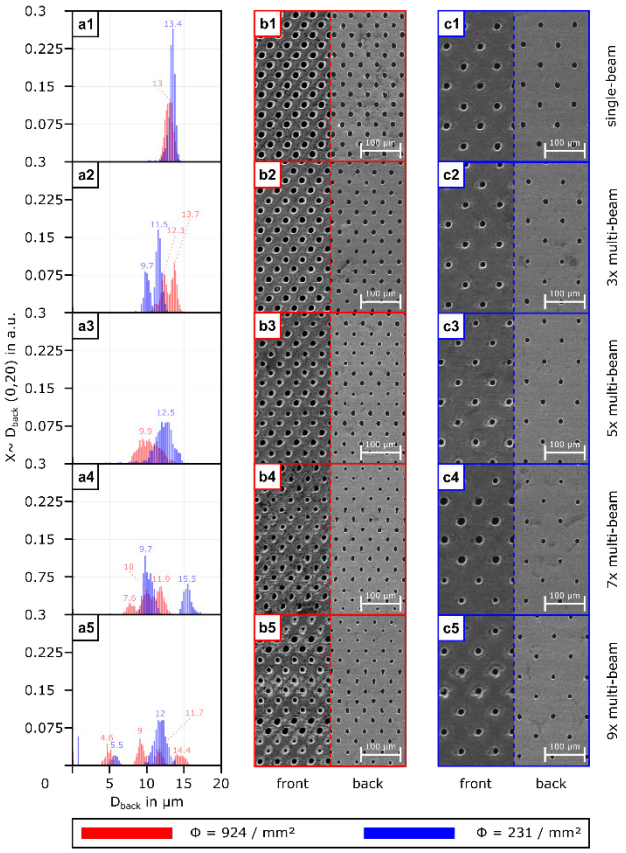

Fig. 10 Influence of different numbers of parallel laser beams and hole density Φ on the shape and absolute distribution of the pierced backside diameter $X{\sim}D_{back}$. Single-beam percussion drilling delivers best results in terms of round hole shapes and even size distributions (a1, b1, b2). Increasing numbers of multi-beams are prone to an inhomogeneous energy distribution from spatial light modulation, resulting in varying hole sizes. Holes sizes are clearly distinguishable as separated maxima in the distribution plots (a1 – a5). This negative effect intensifies for closer hole distances and higher numbers of multi-beams (b4, b5 to c4, c5).

Additionally, modern SLM are capable of withstanding high energy ultrashort pulses for extensive time periods with excellent beam shaping quality [18]. The fundamental working principles of spatial beam shaping for femtosecond laser processing is thoroughly described elsewhere [19]. For single-beam operation no phase shift was applied, causing the SLM to function as a second surface mirror. When phase-patterns for multi-beams were utilized, an aperture within the intermediate focal-plane of the 4f-setup (cf. Fig. 1) was used to filter higher orders of diffraction. The symmetrical line-shaped hole arrangement of these patterns was always centralized around the 0^{th} order of diffraction (cf. Fig. 2, a2). Fig. 10 shows a comparison between single-beam and multi-beam percussion drilling with up to 9 parallel beams. Images a1 – a5 show the relative distribution of backside hole diameters within an area of around 1.1 mm^2 with two different hole densities of 924 mm^{-2} (b1 – b5) and 231 mm^{-2} (c1 – c5). Corresponding SEM images (b_i, c_i) show both front- and backside of the drilled titanium foil. Pulse energy $E_p = 0.8\,\mu J$, base frequency $f_{base} = 25\,kHz$ and burst frequency $f_{burst} = 2.5\,GHz$ were chosen as optimal parameters, determined in section 3.3. A total of $N_p = 3500$ consecutive pulses equal to a drilling time of $T_{drill} = 14\,ms$ were applied to each drilling cycle. The expected backside hole diameter of $D_{back} = 12.6\,\mu m$ from a previous experiment (cf. Fig. 8) is in good accordance with the central peak position of the hole diameter distribution for single-beam processing (a1). Single-beam processing for a low hole density (a1, blue) shows the least variance between hole diameters, evident as only one narrow peak in the absolute distribution. Increasing hole density (a1, red) reveals broadening of the peaks, presumably from a dynamic interaction between emerging bubbles on a microsecond timescale for irradiation areas of small spatial separation, thoroughly investigated in comparable studies for ablation in liquids [20; 21]. For increasing numbers of parallel beams, a tendency for broadening and separation into multiple peaks is observed. This can be attributed to an inhomogeneous intensity-distribution from a non-ideal phase pattern. A possible solution for better intensity homogenization in a future implementation is to use an active feedback-loop from a beam-profiler placed in a second intermediate focal plane, decoupled by a plate beamsplitter placed between the first two dielectric mirrors (cf. Fig. 1). Implementing this measure could further improve iterative phase pattern calculations for an increased number of intensity-homogenized multi-beams. Additionally, a more advanced filtering method by an asymmetric mask instead of a simple aperture could be used during processing to block the centralized 0^{th} order of diffraction.

While precise micromachining of small structures oftentimes is a challenge on its own, upscaling to large area machining poses additional hurdles in terms of multi-system integrity and the combined positioning accuracy of all axes. For this reason, a custom centralized operation software controlled every aspect of the system, including the laser, galvo-scanner, pumps, mechanical axes, and auxiliary components (cf. section 2). In automatic mode, instructions from customizable files were processed by the software, while continuous status feedback from all components

guaranteed a successful interplay of all components. The positional system itself was configured as a hierarchical structure with the comparably slow mechanical-axes at its top, followed by the scanner- and laser-system. The former were solely used for semi-dynamic coarse positioning of the fluidic chamber and optical assembly, meaning that a target position could be precisely set and maintained, but without a dynamic synchronization of the galvo-scanner's deflection angles. The reason for the implementation of a combined system lies within the limited field-size of the telecentric f-theta lens. In general, a small operational field-size of the scanner is preferred in favor of positional accuracy and prevention of wavefront-distortions. Since hole-to-hole distances can be as small as a few tens of micrometers, retrofitted high accuracy linear sensors on all axes guaranteed an absolute positioning error below 2 micrometers. This measure was crucial, since multiple fields that are processed by the laser scanner must be precisely intermeshed with each other along adjacent edges. Even the slightest misalignment along a small section of a single field may cause holes to overlap and ultimately compromising the whole structure. Fig. 11 shows the principle of generating large patterns, both with single- and multi-beam drilling strategies. For single-beam drilling (a2), sequencing was performed in offset rows (a1). For multi-beam drilling all beams were vertically aligned with a constant distance to each other (b2). To maximize hole density, sequencing was set up with a variable number of intermediate holes between two beams, exemplarily shown in (b1). After completion of a processed field, the fluidic chamber was translated to the next position (c). Both scanner and axes movements were always oriented in the opposite or orthogonal direction of the liquid flow to reduce interference with ablated particles and bubbles. The successful results from automatic large area drilling are displayed in Fig. 12 as backlit grayscale images. Near-seamless intermeshing of a 2×2 stitching configuration for all multi-beam phase patterns under the same parameters chosen in section 4 was achieved (a).

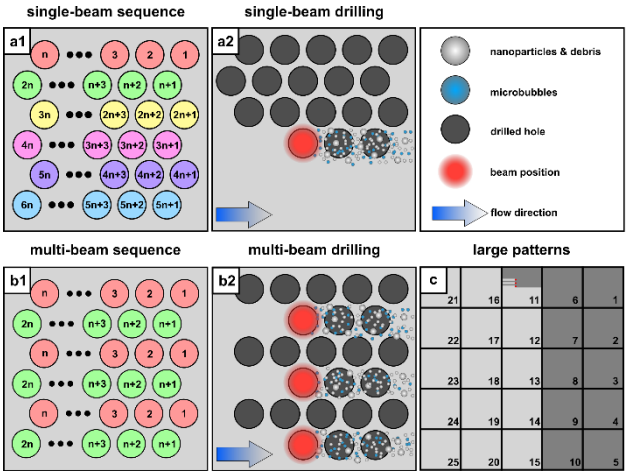

Fig. 11 Ablation and field-stitching sequences of single- and multi-beam processing for small (a, b) and large (c) seamlessly intermeshed areas. Small area sequencing of single-beam drilling (a2) is performed row by row (a1), whereas multi-beam drilling (b2) is offset by half of the distance between two sub-beams (b1). Micromachining of larger areas is done by seamless intermeshing of smaller sections. Both movements from scanner (a, b) and axis (c) are performed in the opposite direction of the flowing liquid.

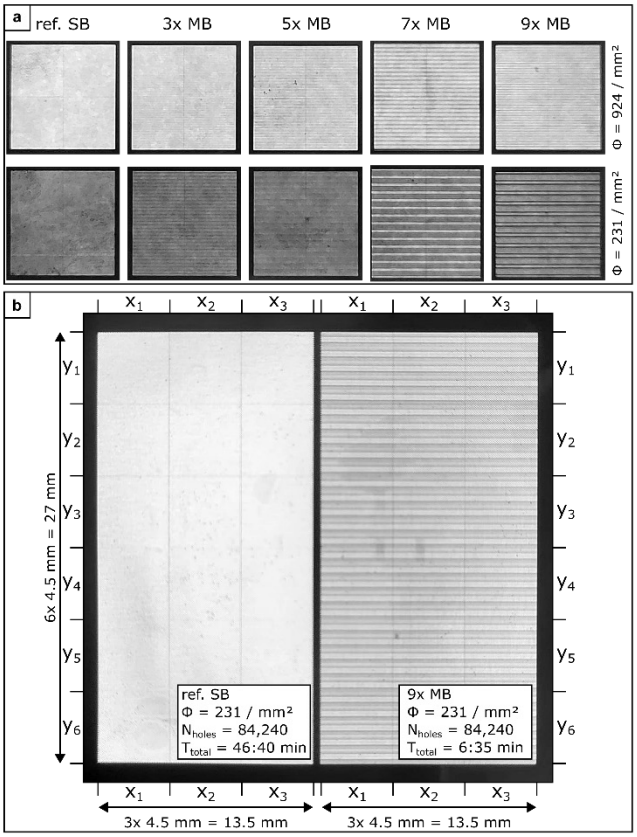

Fig. 12 Backlit grayscale images from large area single- and multi-beam laser percussion drilled titanium foils by automatic intermeshed stitching. Different hole densities Φ and number of parallel multi-beams were tested in a 2×2 stitching configuration of 9×9 mm^2 total size (a). A direct comparison between single- and 9x multi-beam drilling in a 3×6 stitching configuration on the same foil can be seen in (b). Due to an inhomogeneous intensity distribution by an unoptimized phase pattern algorithm (cf. section 4), varying hole sizes appear as horizontal lines with varying color gradient.

In contrast to software- or physics-related improvements (cf. section 3), the total processing time for multi-beam drilling of homogenous hole distributions behaves almost directly anti-proportional to the number of multi-beams. Between single- and 9x multi-beam processing, a total time reduction of 85.8 % is reported. Regarding the total number of drilled holes, a rate of 213 holes per second is achieved. Drilling of smaller hole size with shorter drilling times suggests rates close to 300 per second. When using single-beam operation, the energy efficiency of the system was determined to 0.906, as a factor of the maximum power directly after the polarizing beamsplitter cube and after the f-theta lens. While using a diffraction pattern of nine multi-beams, this value further decreased to its lowest value of 0.876 . While all optical components are designed to withstand constant operation with the maximum pulse energy of around 400 µJ at 100 kHz repetition rate, the diffraction efficiency of the SLM will supposedly further decrease for higher number of multi-beams. In disregard of the declining diffraction efficiency, a hypothetical configuration of the current system could be upscaled to around 43 multi-beams when using optimal parameters derived from section 4.

5. Conclusion

In this study, ultrashort pulsed laser percussion drilling of 25 micrometer thin foils of grade 1 titanium immersed in flowing deionized water was investigated. First, a thorough investigation of the process was performed for conventional single-beam irradiation, characterizing an optimal processing window at low pulse energies between $E_p = [0.05\ 1.5]$ µJ, with minimized influence from non-linear effects such as self-focusing and plasma formation. With a tendency towards lower pulse repetition rates, the influence of different frequencies was almost negligible in terms of temporal process efficiency. Hereupon the study was extended by choosing a low base frequency and introducing varying numbers of high frequency nano- and picosecond burst-trains, to artificially modulate the frequency within a short time interval. Both 63 MHz and 2.5 GHz burst frequencies showed significant improvements over conventional pulsed operation. The best results were achieved at a very low base frequency of just 25 kHz by selecting every fourth pulse from the lowest available resonator frequency of 100 kHz and the largest available number of ten consecutive bursts at 2.5 GHz. Each burst pulse delivered the same energy of 0.8 µJ, resulting in exit hole diameters between 2 µm and 22 µm, depending solely on the number of pulses applied. As a remarkable side effect, the roundness of the hole and the aspect ratio between the entrance and exit sides were significantly improved by using burst-modes. This can be explained by the temporal separation between the early electron gas excitation with subsequent lattice thermalization on a femtosecond to tens of picoseconds timescale and the much later appearance of pressure waves and cavitation bubbles after a few nanoseconds. Therefore, it can be assumed that the combination of ten ultrashort pulses applied within a very short time frame of about 3.6 ns and long intermediate time intervals of 40 µ s between burst trains effectively minimized interactions between laser radiation, pressure waves and cavitation bubbles. For more efficient use of the available energy, process parallelization was demonstrated by multi-beam generation with a high-power spatial light modulator. Successful implementation of 9 parallel multi-beams with up to 924 holes per mm^2 over an intermeshed area of 360 mm^2 is reported, reducing the total processing time by 85.8 % compared to single-beam operation. Comparative results from the fabrication of even larger meshed areas up to 2500 mm^2 mark the current technical limit of the presented system.

Future enhancements using active feedback phase pattern generation could enable a further increase in the number of multi-beams, pushing towards the maximum power capability of the laser system. With the given parameters, hypothetical upscaled drilling rates above 1000 s^{-1} are conceivable. Size limitations from the fluidic chamber could be bypassed by implementing roll to roll processing in combination with a fast polygon scanner unit, ideally suited for thin foil-based materials, like presented in this study.

Acknowledgments

This project was supported by the Federal Ministry of Economic Affairs and Climate Action (IGF project no.: 21971N

References

[1] C. Lutz, J. Helm, K. Tschirpke, C. Esen, and R. Hellmann: Mater., 16, (2023) 5775.

[2] J. Neddersen, G. Chumanov, and T. M. Cotton: Appl. Spectrosc., 47, (1993) 1959.

[3] D. Zhang, B. Gökce, and S. Barcikowski: Chem. Rev., 117, (2017) 3990.

[4] C. Lutz, G. Roth, S. Rung, C. Esen, and R. Hellmann: J. Laser Micro/Nanoeng., 16, (2021) 62.

[5] C. Lutz, S. Schwarz, J. Marx, C. Esen, and R. Hellmann: Photonics, 10, (2023) 413.

[6] Ö. F. Selamet, F. Becerikli, M. D. Mat, and Y. Kaplan: Int. J. Hydrogen Energy, 36, (2011) 11480.

[7] P. Maack, C. Günther, K. Bargon, A. Kanitz, C. Esen, and A. Ostendorf: J. Laser Micro/Nanoeng., 1, (2024) 1.

[8] J. M. Liu: Opt. Lett., 7, (1982) 196.

[9] E. Nibbering, M. A. Franco, B. S. Prade, G. Grillon, C. Le Blanc, and A. Mysyrowicz: Opt. Commun., 119, (1995) 479.

[10] J. H. Marburger: Prog. Quantum Electron., 4, (1975) 63.

[11] A. Kanitz, M.-R. Kalus, E. L. Gurevich, A. Ostendorf, S. Barcikowski, and D. Amans: Plasma Sources Sci. Technol., 28, (2019) 103001.

[12] S. Dittrich, M. Spellauge, S. Barcikowski, H. P. Huber, and B. Gökce: Opto-Electron. Adv., 5, (2022) 210053.

[13] M. Spellauge, C. Doñate-Buendía, S. Barcikowski, B. Gökce, and H. P. Huber: Light Sci. Appl., 11, (2022) 68.

[14] H. Vaghasiya, S. Krause, and P.-T. Miclea: Opt. Mater. Express, 13, (2023) 982.

[15] A. Žemaitis, P. Gečys, and M. Gedvilas: Adv. Eng. Mater., (2024) 1.

[16] P. Balage, M. Lafargue, T. Guilberteau, G. Bonamis, C. Hönninger, J. Lopez, and I. Manek-Hönninger: Micromachines, 15, (2024) 632.

[17] P. Balage, J. Lopez, G. Bonamis, C. Hönninger, and I. Manek-Hönninger: Int. J. Extrem. Manuf., 5, (2023) 15002.

[18] Y. Tang, Q. Li, Z. Fang, O. J. Allegre, Y. Tang, W. Perrie, G. Zhu, D. Whitehead, J. Schille, U. Loeschner, D. Liu, L. Li, S. P. Edwardson, and G. Dearden: Opt. Laser Technol., 181, (2025) 111589.

[19] Y. Hayasaki and S. Hasegawa: "Ultrafast Laser Nanostructuring - Spatial Beam Shaping with a Liquid-Crystal Spatial Light Modulator for Surface Micro- and Nanoprocessing" ed. by R. Stoain and J. Bonse, (Springer Series in Optical Sciences, 2023) 533.

[20] F. Riahi, A. Bußmann, C. Doñate-Buendia, S. Adami, N. A. Adams, S. Barcikowski, and B. Gökce: Photon. Res., 11, (2023) 2054.

[21] F. Riahi, C. Doñate-Buendia, S. Barcikowski, and B. Gökce: Part. Part. Syst. Char., 41, (2024) 1.

(Received: June 28, 2024, Accepted: October 20, 2024)